



# Noble metal modified reduced graphene oxide/TiO<sub>2</sub> ternary nanostructures for efficient visible-light-driven photoreduction of carbon dioxide into methane

Lling-Lling Tan<sup>a</sup>, Wee-Jun Ong<sup>a</sup>, Siang-Piao Chai<sup>a,\*</sup>, Abdul Rahman Mohamed<sup>b</sup>

<sup>a</sup> Multidisciplinary Platform of Advanced Engineering, Chemical Engineering Discipline, School of Engineering, Monash University, Jalan Lagoon Selatan, 46150 Bandar Sunway, Selangor, Malaysia

<sup>b</sup> Low Carbon Economy (LCE) Group, School of Chemical Engineering, Universiti Sains Malaysia, Engineering Campus, Seri Ampangan, 143000 Nibong Tebal, Pulau Pinang, Malaysia

## ARTICLE INFO

### Article history:

Received 5 September 2014

Received in revised form

11 November 2014

Accepted 18 November 2014

Available online 25 November 2014

### Keywords:

Photocatalyst

Noble metal

Titanium dioxide

Graphene

Carbon dioxide

## ABSTRACT

The design and architecture of visible-light-active photocatalysts is a key aim among material scientists for the efficient utilization of renewable solar energy. In this paper, a series of noble metal (Pt, Pd, Ag and Au) nanoparticles supported on reduced graphene oxide/TiO<sub>2</sub> (GT) were successfully synthesized through a dual step process. In the first step, GT nanocomposites were prepared using a solvothermal method. The as-prepared hybrid nanostructures were subsequently employed as supporting materials for the dispersion of metal nanoparticles. A simple polyol process was used to respectively reduce metal ions (PtCl<sub>6</sub><sup>2-</sup>, Pd<sup>2+</sup>, Ag<sup>+</sup>, and AuCl<sub>4</sub><sup>-</sup>) into metal (Pt, Pd, Ag and Au) nanoparticles on GT. The three-component nanocomposites exhibited enhanced photocatalytic activities toward the photoreduction of CO<sub>2</sub> into CH<sub>4</sub> gas under the irradiation of typical daylight bulbs. This was attributed to the multiplex phenomena such as an enhanced utilization of visible light, efficient electron transfer in the noble metal-doped GT nanojunctions and interfacial electron transfer in the reduced graphene oxide (rGO) sheets, as evidenced by UV–vis and PL characterizations. Among the noble metals studied, the Pt-doped GT nanocomposites showed the highest efficiency in reducing CO<sub>2</sub>. A total CH<sub>4</sub> yield of 1.70 μmol/g<sub>cat</sub> was achieved after 6 h of light irradiation, which was 2.6 and 13.2 folds higher in comparison to GT and commercial P25, respectively. Based on the experimental results obtained, a plausible mechanism for the photocatalytic process associated with Pt-GT was proposed.

© 2014 Elsevier B.V. All rights reserved.

## 1. Introduction

The past few decades have witnessed a significant increase in atmospheric carbon dioxide (CO<sub>2</sub>) levels as a result of fossil fuel combustion. Furthermore, the depletion of hydrocarbon fuels is an inevitable problem which has to be faced in the near future [1]. To address these issues, a desirable strategy is to recycle and convert CO<sub>2</sub> into fuels or other useful chemicals. To this end, the reduction of CO<sub>2</sub> remains to be an energy intensive challenge owing to the high kinetic and thermodynamic stability of CO<sub>2</sub> [2]. The development of an efficient photocatalyst is a compelling approach to meet this challenge, and there has been a prominent quest to convert CO<sub>2</sub> into hydrocarbon fuels [3,4]. The photocatalytic process can be

sustainable by harnessing solar energy, which renders it environmentally benign and economically viable. Anatase titanium dioxide (TiO<sub>2</sub>) has been widely studied as a state-of-the-art semiconductor photocatalyst because of its long-term stability against photo- and chemical corrosion, low cost, non-toxicity as well as strong oxidizing and reducing power [5–8]. However, TiO<sub>2</sub> has a relatively wide band gap energy of 3.2 eV, at which it only absorbs radiation in the ultraviolet (UV) region, which represents 5% absorption of the solar spectrum. Therefore, the photoactivity of TiO<sub>2</sub> can be significantly improved if it absorbs light in the visible region (≈47% of solar energy), in addition to the small fraction of UV [9]. Simultaneously, the separation of photoexcited electron–hole pairs and their migration to the surface reaction sites also play a distinct role in ensuring high photocatalytic activity [10]. In general, most photogenerated charge carriers have the tendency to undergo rapid recombination before taking part in chemical reactions [11]. Therefore, it is of great importance to develop new strategies

\* Corresponding author. Tel.: +60 3 5514 6234; fax: +60 3 5514 6207.  
E-mail address: [chai.siang.piao@monash.edu](mailto:chai.siang.piao@monash.edu) (S.-P. Chai).

for a more efficient  $\text{TiO}_2$ -based photocatalyst which could utilize the visible light portion of sunlight and facilitate charge separation.

Graphene, a new class of carbon material comprising of single-atom-thick  $\text{sp}^2$  hybrid carbon atoms, has garnered tremendous research interest owing to its intriguing characteristics [12–17]. In the case of graphene-hybridized materials, graphene can serve as a potential sink for electrons and act as an efficient electron transporting bridge due to its high electron mobility and extended  $\pi$ -electron conjugation [18–22]. The heterojunction formed at the interface of both materials separates the photoexcited electron–hole pairs and suppresses the recombination process [23]. To date, graphene– $\text{TiO}_2$  and/or rGO– $\text{TiO}_2$  composites have received considerable attention due to their enhanced photocatalytic performance [24–29]. In a recent report from our research group, we demonstrated the effective integration of  $\text{TiO}_2$  nanoparticles on reduced graphene oxide (rGO) sheets through a one-step solvothermal route. The composite was shown to display high efficiency toward the photoreduction of  $\text{CO}_2$  into  $\text{CH}_4$  gas under visible light irradiation [24]. However, there is still room to increase the photocatalytic activity of the composites by further promoting light absorption and suppressing the charge recombination rate through the incorporation of other active components into the binary composites [30–32].

The dispersion of noble metal co-catalysts such as Pt, Pd, Ag and Au on semiconductor particles have been demonstrated to enhance the photocatalytic conversion of  $\text{CO}_2$  with  $\text{H}_2\text{O}$  into hydrocarbon fuels [33–36]. It is generally accepted that the metal clusters play a threefold role in the improved efficiency: (i) impede electron–hole recombination by trapping photogenerated conduction band electrons; (ii) enhance photoreduction efficiency owing to Fermi level equilibration and (iii) provide thermal catalytic sites for adsorbed species and reaction intermediates [37,38]. Moreover, noble metal nanoparticles may possess a localized surface plasmon resonance (LSPR) phenomenon which enables them to exhibit strong and broad absorption in the visible region of the solar spectrum [10]. Correspondingly, the combination of noble metals and graphene with the ternary nanocomposite of  $\text{TiO}_2$  is expected to facilitate its photocatalytic performance in various applications. While there has been quite a few researches concerning the use of rGO/ $\text{TiO}_2$  [24,39] and noble metal-doped  $\text{TiO}_2$  photocatalysts [34,40], to the best of our knowledge, there is no prior study on the application of noble metal-modified rGO/ $\text{TiO}_2$  (NM-GT) ternary nanostructures in the photoconversion of  $\text{CO}_2$ .

In our previous work, titanium(IV) butoxide and graphene oxide were used as starting materials to yield GT nanocomposites through a one-pot solvothermal process [24,41]. Herein, we use this composite to construct NM-GT ternary nanostructures through a simple polyol method, without employing toxic and harsh reducing agents such as hydrazine and sodium borohydride. A two-step synthetic route for preparing NM-GT was chosen as it is difficult to manipulate the simultaneous homogenous growth of two or more particles on rGO sheets [42]. In the polyol process, ethylene glycol was used as both the solvent and reducing agent for the additive metal ions ( $\text{PtCl}_6^{2-}$ ,  $\text{Pd}^{2+}$ ,  $\text{Ag}^+$ , and  $\text{AuCl}_4^-$ ) to form metal (Pt, Pd, Ag and Au) islands on the surface of  $\text{TiO}_2$  and rGO. Finally, four ternary composites were prepared and designated as Pt-GT, Pd-GT, Ag-GT and Au-GT. Among the samples, Pt-GT displayed the highest efficiency for the reduction of  $\text{CO}_2$  into  $\text{CH}_4$  gas under the irradiation of low-power, energy saving daylight bulbs. The intense interaction between different components of the composites resulted in an efficient separation and transmission of photoinduced electron–hole pairs as well as an improved utilization rate of visible light [43]. These findings could provide some insights on the design of triple heterostructures and its application for future research work in photocatalysis.

## 2. Experimental

### 2.1. Materials

Graphite powder, titanium(IV) butoxide (TBOT) 97%, ethylene glycol (EG) 99%, acetic acid (HAc) 99.7%, Degussa P25 99.5%, anatase  $\text{TiO}_2$  99.7%, silver nitrate ( $\text{AgNO}_3$ ) 99.9%, palladium(II) nitrate dehydrate ( $\text{Pd}(\text{NO}_3)_2 \cdot 2\text{H}_2\text{O}$ ) 40% Pd basis, and gold(III) chloride trihydrate ( $\text{HAuCl}_4 \cdot 3\text{H}_2\text{O}$ ) 99.9% were supplied by Sigma Aldrich. Hexachloroplatinic(IV) acid hexahydrate ( $\text{H}_2\text{PtCl}_6 \cdot 6\text{H}_2\text{O}$ ) 99.9% was supplied by Acros Organics. Ethanol (96%) was supplied by Chemolab. All chemicals were of analytical reagent grade and were used as received without further purification.

### 2.2. Synthesis of GT nanocomposites

The synthesis was carried out according to our previous work [24]. Graphite oxide (prepared by a modified Hummers' method) [44] was dispersed into deionized (DI) water and ultrasonicated for 1 h at 40 kHz and 180 W to produce graphene oxide (GO) sheets. The resultant dispersion was then chilled to  $5^\circ\text{C}$  in an ice bath. Meanwhile, a titanium precursor composed of 1.5 mL TBOT, 7.21 mL EG and 1.14 mL HAc was also chilled to  $5^\circ\text{C}$ . The mixture was then added dropwise into the chilled GO aqueous solution under vigorous stirring. Subsequently, the GO/ $\text{TiO}_2$  stock solution was transferred into a 200 mL Teflon-lined stainless steel autoclave and was kept at  $180^\circ\text{C}$  for 8 h. After the solvothermal treatment, the reaction system was cooled naturally to ambient temperature. The resulting gray precipitate was harvested by centrifugation at 5000 rpm for 30 min and washed thoroughly with ethanol three times to remove undecorated  $\text{TiO}_2$  particles, unreacted chemicals and residual EG. Finally, the product was dried in an oven at  $70^\circ\text{C}$  overnight before characterization. Pure  $\text{TiO}_2$  was synthesized using a similar approach without the addition of GO.

### 2.3. Synthesis of NM-GT ternary nanocomposites

All NM-GT ternary composites were synthesized using a polyol process. For platinum-doped GT (Pt-GT) composites, GT was first dispersed in EG by ultrasonication. Then, a pre-determined amount of Pt precursor ( $\text{H}_2\text{PtCl}_6 \cdot 6\text{H}_2\text{O}$ ) dissolved in EG was added slowly under magnetic stirring. The mixed solution was subsequently refluxed in a two-necked round bottom flask fitted in a heating mantle under continuous magnetic stirring at  $140^\circ\text{C}$  for 2 h. After cooling to room temperature, the as-synthesized Pt-GT composite was harvested by centrifugation at 8000 rpm for 30 min and washed thoroughly with DI water three times. Finally, the product was dried in an oven at  $70^\circ\text{C}$  overnight before characterization. Similarly, Pd-GT, Ag-GT and Au-GT samples were prepared using the same procedure except for the addition of  $\text{Pd}(\text{NO}_3)_2 \cdot 2\text{H}_2\text{O}$ ,  $\text{AgNO}_3$  and  $\text{HAuCl}_4 \cdot 3\text{H}_2\text{O}$ , instead of  $\text{H}_2\text{PtCl}_6 \cdot 6\text{H}_2\text{O}$ , respectively. The loading of each respective noble metal on the GT hybrid support was controlled to be 2.0 wt.%. Fig. 1 shows the reaction procedure for the two-step synthesis of NM-GT ternary nanocomposites. Pt- $\text{TiO}_2$  binary nanocomposites were also prepared using the same method except for the addition of pure  $\text{TiO}_2$  instead of GT.

### 2.4. Materials characterization

The surface morphology and elemental composition of all samples were analyzed by a field emission scanning electron microscopy (FESEM) (Hitachi SU8010) equipped with an Oxford-Horiba Inca XMax50 energy dispersive X-ray (EDX). The specimen for FESEM analysis was prepared by depositing a drop of diluted suspension in ethanol on a silicon wafer. High resolution transmission electron microscopy (HRTEM) images were taken with a JEOL

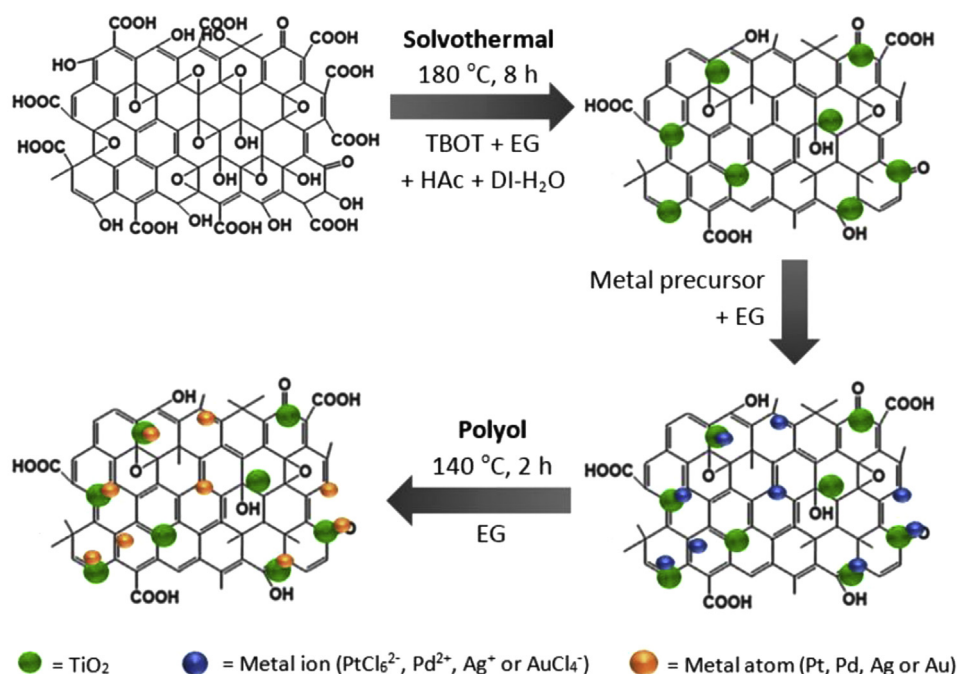


Fig. 1. Schematic illustrating the synthesis of NM-GT ternary composites by a two-step routine.

JEM-2100F microscope operating at 200 kV. TEM samples were prepared by depositing a drop of diluted suspension in ethanol on a lacey-film-coated copper grid. X-ray diffraction (XRD) patterns were obtained on a Bruker D8 Discover X-ray diffractometer using Ni-filtered Cu-K $\alpha$  radiation ( $\lambda = 0.154056$  nm) at a scan rate of  $0.02^\circ \text{ s}^{-1}$ . The accelerating voltage and applied current were 40 kV and 40 mA, respectively. Ultraviolet–visible (UV–vis) absorbance spectra were obtained using a UV–vis spectrophotometer (Agilent, Cary 100) equipped with an integrated sphere. The absorbance spectra were analyzed under ambient temperature in the wavelength ranging from 200 to 800 nm. The band gap energies of the photocatalysts were estimated from the Kubelka–Munk (KM) function,  $F(R)$  and the extrapolation of the Tauc plot  $[F(R) \cdot h\nu]^{1/2}$  to the abscissa of photon energy,  $h\nu$ . Photoluminescence (PL) measurements were carried out with a fluorescence spectrophotometer (LS 55, Perkin Elmer). The excitation wavelength was 320 nm, with a scanning speed of 500 nm/min. The widths of the excitation and emission slits were fixed at 10 nm.

### 2.5. Evaluation of photocatalytic activity

The photocatalytic activities of the developed NM-GT ternary nanocomposites were studied in a CO<sub>2</sub> photoreduction system at ambient condition in a continuous gas flow reactor as reported in our previous work [3,24]. The CO<sub>2</sub> photoreduction process was performed under visible light irradiation with a maximum light intensity of 15 W using an energy-saving daylight bulb (Philips, TORNADO 15 W WW E27 220–240 V 1CT). The as-prepared photocatalysts were coated onto glass rods and loaded into quartz tubes, which were then placed under the visible light for irradiation. Upon loading the photocatalyst-coated glass rods, highly pure CO<sub>2</sub> (99.99%) was bubbled through water to produce a mixture of CO<sub>2</sub> and water vapour, which acted as a sacrificial reagent, into the photoreactor at atmospheric pressure. Before switching on the light source, wet CO<sub>2</sub> was allowed to flow through the photoreactor at 30 mL/min for 30 min to remove any excess air and to ensure the complete adsorption of gas molecules. After the purging process, the light source was switched on and the

CO<sub>2</sub> photoreduction process was conducted at 5 mL/min using a mass flow controller. The average intensity of the light source was measured to be  $8.5 \text{ mW cm}^{-2}$  by using a pyranometer (Kipp and Zonen type CMP 6). The light spectrum of the light source was recorded using an Avantes fiber optic spectrometer (AvaSpec-128) equipped with a cosine collector (Fig. S3 in Supplementary Material). The distance between the light source and the photoreactor was measured to be about 5 cm. The product gas generated from the CO<sub>2</sub> photoreduction process was collected at 1-h intervals and was analyzed by a gas chromatography (GC) (Agilent 7890A) equipped with a flame ionized detector (FID). The entire photoreaction system was enclosed within a black box to avoid any interference of light source from the surrounding. The total yield of methane (CH<sub>4</sub>) gas was calculated using Eq. (1). To confirm the visible-light-activity of the optimized photocatalyst, the CO<sub>2</sub> photoreduction experiment was repeated under the irradiation of a Xenon arc lamp (Model no: CHF XM500 W) with a UV cut-off filter ( $\lambda > 400$  nm) (Figs. S8 and S9 in Supplementary Material).

$$\text{Total CH}_4 \text{ yield} = \frac{\text{total amount of CH}_4 \text{ produced } (\mu\text{mol})}{\text{amount of photocatalyst used (g-catalyst)}} \quad (1)$$

## 3. Results and discussion

### 3.1. Characterizations of NM-GT ternary nanocomposites

The morphology and structural features of the NM-GT composites were elucidated by TEM and HRTEM. Fig. 2 displays the representative TEM images for the ternary hybrid nanostructures at low (Fig. 2A–D) and high magnifications (Fig. 2E–H). It is evident that the metal nanoparticles were well dispersed on the GT hybrid support without noticeable agglomeration. The darker regions corresponded to the noble metals and the lighter ones to the anatase TiO<sub>2</sub> nanoparticles. All metal nanoparticles exhibited a narrow size distribution on the GT support and the average particle sizes of Pt, Pd, Ag and Au were calculated to be 3.8, 5.0, 5.2 and 5.1 nm, respectively. Fig. 2E–H shows the HRTEM images of the ternary composites, in which the synthesized noble metal nanoparticles



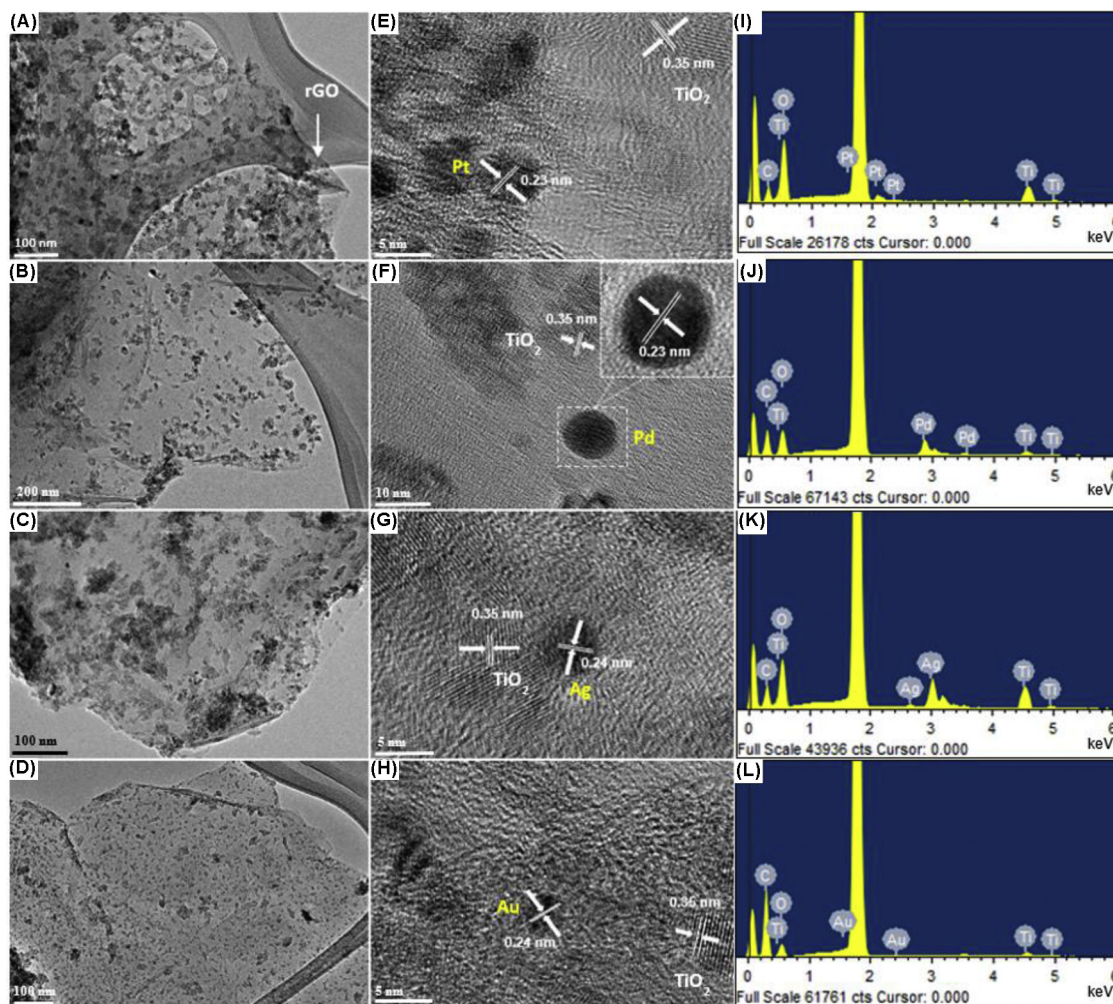


Fig. 2. Typical TEM, HRTEM and EDX characterizations of (A, E, I) Pt-GT, (B, F, J) Pd-GT, (C, G, K) Ag-GT and (D, H, L) Au-GT ternary nanocomposites, respectively.

and  $\text{TiO}_2$  can be clearly identified by the lattice fringes. The lattice spacing of Pt, Pd, Ag and Au nanocrystals were measured to be about 0.23, 0.23, 0.24 and 0.24 nm, respectively, all of which corresponded to the (1 1 1) crystal planes of Pt, Pd, Ag and Au [38,45–47]. This confirmed that the darker spots seen from the TEM images were the relevant metal nanoparticles. The existence of noble metal nanoparticles was further evidenced by EDX and XRD measurements. For all NM-GT samples, the lattice spacing of  $\text{TiO}_2$  was measured to be ca. 0.35 nm, which corresponded to the (1 0 1) plane of anatase  $\text{TiO}_2$  [48]. The elemental analysis of the NM-GT composites was carried out using EDX, as shown in Fig. 2I–L. In overall, the C element originated from the rGO sheets, while the Ti and O elements were from the  $\text{TiO}_2$  nanoparticles. The strong  $K\alpha$  and  $K\beta$  peaks from Ti element appeared at 4.5 and 4.9 keV with a moderate  $K\alpha$  peak from O element at 0.54 keV [49]. Fig. 2I–L also confirmed the presence of Pt, Pd, Ag and Au in the NM-GT composites with their respective peaks.

XRD analysis was performed to study the crystal phases of the as-synthesized NM-GT nanocomposites (Fig. 3). All samples exhibited the characteristic (1 0 1), (0 0 4), (2 0 0), (1 0 5), (2 1 1), (2 0 4), (1 1 6), (2 2 0), and (2 1 5) crystal planes of a pure tetragonal anatase phase (space group:  $I4_1/amd$ , JCPDS No. 21-1272) with lattice constants  $a = 3.78 \text{ \AA}$  and  $c = 9.50 \text{ \AA}$  [50,51]. This confirmed that the crystal structure of  $\text{TiO}_2$  was not altered by the addition of noble metals. By applying the Scherrer's equation, the average crystallite size of  $\text{TiO}_2$  in the NM-GT samples were also found to be close to

that of the  $\text{TiO}_2$  on the GT composite (Table 1). This indicated that the incorporation of noble metals did not result in any changes to the crystallite size of  $\text{TiO}_2$  on the rGO sheets. The observed peaks corresponding to the (1 1 1), (2 0 0), (2 2 0) and (3 1 1) facets of Pt, Pd, Ag and Au could all be assigned (JCPDS 65-2868, 05-0681, 04-0783 and 65-2870, respectively) [48,52–54]. This demonstrated that Pt, Pd, Ag and Au nanoparticles were all composed of pure crystalline with the face-centered cubic (fcc) structure [52,55]. The intensity ratios of the (2 0 0) peak to the (1 1 1) peak obtained for Pt (0.431), Pd (0.449), Ag (0.410) and Au (0.322) indicated that all the metallic particles were preferentially dominated by (1 1 1) facets.

UV–vis spectroscopic measurements were carried out to examine the optical response of the NM-GT composites (Fig. 4). All the samples studied displayed a typical absorption, with an intense transition in the UV region of the spectra, which was assigned to the intrinsic band gap absorption of  $\text{TiO}_2$  resulting from the

Table 1  
Average size of  $\text{TiO}_2$  in GT, Pt-GT, Pd-GT, Ag-GT and Au-GT.

Sample	Average crystallite size of $\text{TiO}_2$ from XRD (nm)	Average particle size of $\text{TiO}_2$ from HRTEM (nm)
GT	7.92	12.00
Pt-GT	8.09	10.38
Pd-GT	7.42	10.50
Ag-GT	7.68	11.66
Au-GT	8.29	11.46

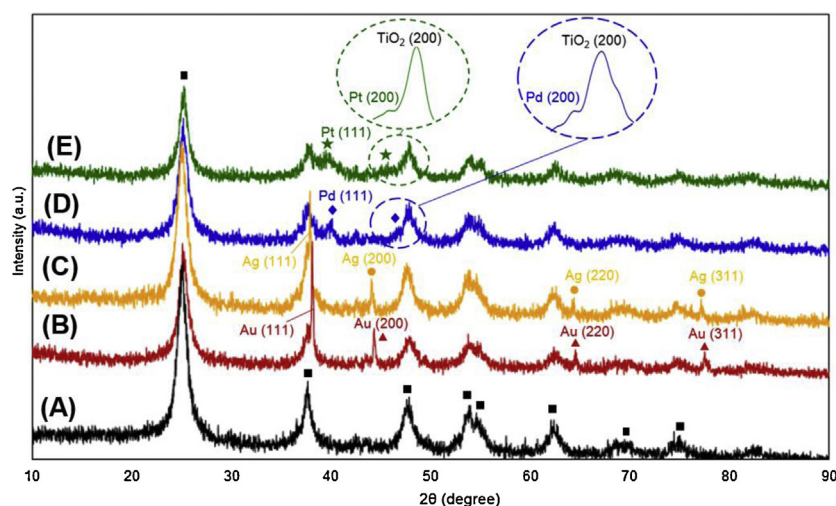


**Fig. 3.** XRD spectra of (A) GT, (B) Au-GT, (C) Ag-GT, (D) Pd-GT and (E) Pt-GT (square, triangle, circle, diamond and star symbols indicate the reflections of the anatase structure of  $\text{TiO}_2$ , and the fcc structures of Au, Ag, Pd and Pt, respectively).

electron transitions from the valence band to the conduction band ( $\text{O}_{2p} \rightarrow \text{Ti}_{3d}$ ) [56]. In comparison to GT, all NM-GT composites not only exhibited an obvious red shift at the absorption edge, but also demonstrated an enhanced absorption in the visible region (Fig. 4A). For Ag-GT and Au-GT composites, an additional absorption peak was observed at 430 and 550 nm, respectively. These peaks could be attributed to the excitation of a surface plasmon in noble metal nanoparticles, which further confirmed the formation of Ag and Au particles on the GT substrate [57]. Similar observations have been reported in literature [42,48,57]. In contrast, no obvious surface plasmon absorption in the visible region was observed for the Pt and Pd-GT samples. It has been established that unlike

coinage metals (e.g. Ag and Au), most potent hydrogenation catalysts such as Pt and Pd, do not display strong plasmon bands in the UV–vis region [58]. This is attributed to the damping effect of the d–d transitions in these metals, which tends to wash out the free electron contribution to the dielectric function [58]. Nevertheless, the Pt-GT and Pd-GT composites are still expected to show enhanced photocatalytic performance as the metal clusters would cause localized energy levels in the band gap of  $\text{TiO}_2$  nanoparticles below the conduction band, where the valence band electrons could be excited at longer wavelengths [59]. A plot of the transformed KM function versus photon energy is shown in Fig. 4B, by which the estimated band gaps are 2.95, 2.40, 2.55, 2.50, and 2.75 eV, corresponding to GT, Pt-GT, Pd-GT, Ag-GT and Au-GT, respectively. This supports the qualitative observation of a red shift in the absorption edge of NM-GT composites as compared to GT. The boosted light absorption for NM-GT nanocomposites in the visible region could enhance the photoexcitation efficiency of  $\text{TiO}_2$ , thus improving its photocatalytic performance. This hypothesis was confirmed by their application in the photocatalytic reduction of  $\text{CO}_2$  under ambient condition.

### 3.2. Photocatalytic properties of NM-GT ternary composites under visible light irradiation

Gas phase photocatalytic reduction of  $\text{CO}_2$  was conducted on the as-prepared NM (Pt, Pd, Ag, Au)-GT nanocomposites under ambient temperature and pressure using a low-power 15 W energy-saving daylight bulb as the visible light source. During the photocatalytic experiments,  $\text{CH}_4$  was detected as the sole product in the outlet gas based on GC analysis. The total yield of  $\text{CH}_4$  gas for 6 h of reaction was calculated and summarized in Fig. 5. The photocatalytic activity of  $\text{CO}_2$  reduction was found to follow the order: Pt-GT > Pd-GT > Ag-GT > Au-GT > GT > P25  $\approx$  anatase  $\text{TiO}_2$ . In addition, a series of control experiments were performed to confirm that the hydrocarbon product was generated through photocatalytic reaction rather than through organic decomposition of the photocatalysts themselves. The control experiments were conducted under the following conditions: (1) in the dark (without light irradiation) with the presence of photocatalyst and  $\text{CO}_2/\text{H}_2\text{O}$  flow, (2) without photocatalyst under  $\text{CO}_2/\text{H}_2\text{O}$  flow and light irradiation, (3) in the absence of  $\text{H}_2\text{O}$  vapor with photocatalyst,  $\text{CO}_2$  flow and light irradiation and (4) under  $\text{N}_2/\text{H}_2\text{O}$  atmosphere in the presence of photocatalyst and light irradiation. In all cases, no appreciable  $\text{CH}_4$  could be detected. This suggested that the products were generated by the

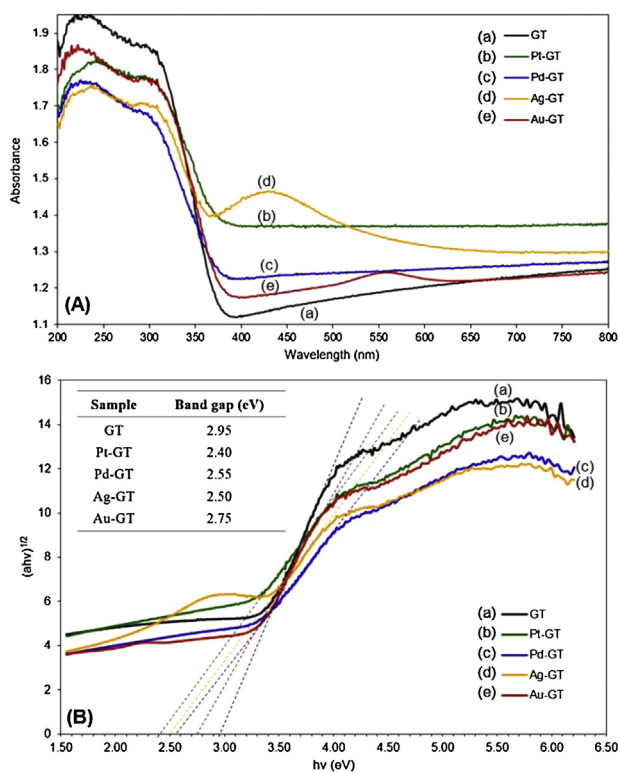


**Fig. 4.** (A) UV–vis diffuse reflectance spectra and (B) corresponding plot of transformed KM function  $[F(R) \cdot hv]^{1/2}$  vs.  $hv$  for GT and NM (Pt, Pd, Ag, Au)-GT composites. (Inset of B) Estimated band gap energies of GT and the NM-GT composites.



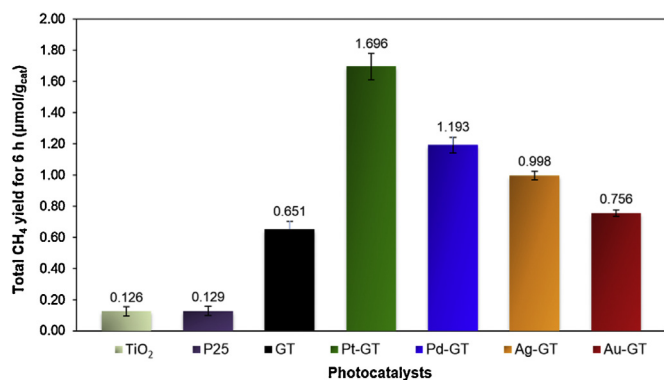


Fig. 5. Total yield of CH<sub>4</sub> over pure anatase TiO<sub>2</sub>, commercial Degussa P25, GT and a series of NM-GT nanocomposites attained after 6 h of reaction.

photocatalytic process and that the presence of photocatalysts, reactant feed (CO<sub>2</sub> and H<sub>2</sub>O) and light irradiation were indispensable for the photoreduction of CO<sub>2</sub>. Among all the studied photocatalysts, pure anatase TiO<sub>2</sub> and P25 exhibited the lowest photocatalytic efficiency for CO<sub>2</sub> reduction due to their limited photoresponse range under visible light irradiation (Fig. S7 in Supplementary Material).

By incorporating rGO sheets, the GT hybrid nanostructure exhibited enhanced photoactivity due to the many unique properties of rGO, *e.g.* its extensive  $\pi$ - $\pi$  conjugation system and excellent conductivity of electrons [13]. The synergistic dyad structure of GT provided access to an optically active charge transfer transition. The conduction band of anatase TiO<sub>2</sub> and the work function of rGO are -4.2 eV [60] and -4.42 eV [61], respectively. Such energy levels were beneficial for the photogenerated electrons to transfer from the TiO<sub>2</sub> conduction band to the rGO sheets, which could effectively separate the charge carriers and hinder electron-hole recombination. In the absence of rGO, most of these charges tend to recombine rapidly without undergoing any chemical reaction. This is primarily due to the adsorption kinetic of the CO<sub>2</sub> molecules (10<sup>-8</sup>–10<sup>-3</sup> s) on TiO<sub>2</sub> being slower than the electron-hole recombination time (10<sup>-9</sup> s) [11,62]. Hence, in the GT composite, rGO served as an electron collector and transporter to effectively separate the photogenerated electron-hole pairs, thus resulting in the photocatalytic enhancement of GT nanocomposites [24].

The NM (Pt, Pd, Ag, Au)-GT ternary composites exhibited a marked enhancement in the photocatalytic activity under visible light irradiation compared to the un-doped GT hybrid support. The enhancement could be correlated to several contributing factors. The formation of heterostructures was believed to play key roles in the highly efficient photocatalytic performance. It is well documented that an effective charge separation/transfer is crucial for the enhancement in photocatalytic activities [63]. The presence of a metal at the surface of TiO<sub>2</sub> would result in the formation of a Schottky barrier at the metal-semiconductor interface. As the Fermi levels of Pt, Pd, Ag and Au [64,65] were lower than that of TiO<sub>2</sub> (Fig. 6), photoexcited electrons could be transferred from the conduction band to the metal particles, while the photogenerated valence band holes remained on TiO<sub>2</sub>. Therefore, the photocatalytic activity could be improved in terms of a longer electron-hole pair separation lifetime. Furthermore, the extended photoresponse range of TiO<sub>2</sub> in the NM-GT composites (Fig. 4) also led to the photocatalytic enhancement.

The experimental results showed that the photocatalytic activity of Pt-GT nanocomposites was the highest among the other NM-GT samples. This is because the photonic efficiency of NM-GT is strongly dependent on electron affinity and the work function of the metal to form a favorable contact with TiO<sub>2</sub> [63]. Pt has higher working function (-5.65 eV) [64] than Au (-5.1 eV), Ag (-4.7 eV)

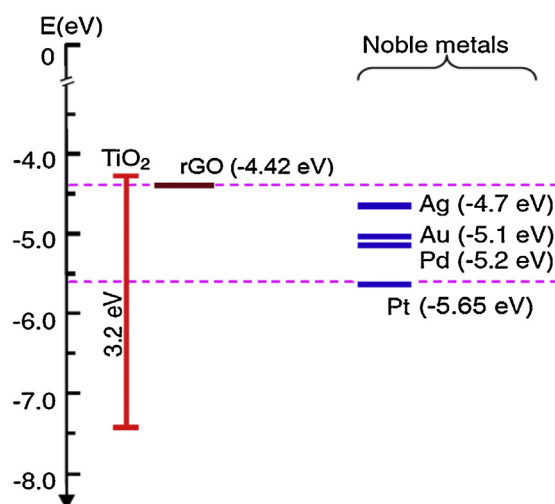
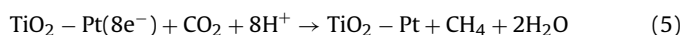
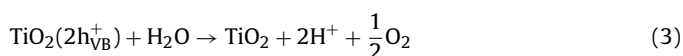


Fig. 6. Energy band positions of rGO, Pt, Pd, Ag and Au, including the conduction and valence bands of TiO<sub>2</sub> photocatalyst.

and Pd (-5.2 eV) [65,66], thus the photogenerated electrons can transfer most efficiently from TiO<sub>2</sub> to loaded Pt nanoparticles, while the reversible process can be extremely difficult. Based on our findings, it can be deduced that the work function of the metal dopant played a dominant role in the enhancement of the ternary nanocomposites, rather than the LSPR effect of the noble metals (Fig. 4A). It should be noted that because the adsorption, transportation and activation of different reactants on metal surfaces are quite different, the effect of each noble metal on the photocatalytic activity may vary with different reactions. For example, the addition of Au was found to be the least effective in our study (Fig. 5) but it showed the best promotive effect in the photocatalytic oxidation of benzene to phenol [67]. Taking Pt-GT as the basis, a plausible photocatalytic mechanism for the reduction of CO<sub>2</sub> was proposed, as shown in Fig. 7. TiO<sub>2</sub> photocatalyst was first excited by the irradiation light to generate electrons at the conduction band and holes at the valence band. Since Pt nanoparticles trap electrons very effectively [68], the photoexcited electrons would migrate and reside on the Pt nanoparticles, where the photoreduction of adsorbed CO<sub>2</sub> would take place (path 1 in Fig. 7). In the case where Pt was deposited onto the rGO sheets, the photoexcitation of TiO<sub>2</sub> first occurred, which led to the generation of electrons and holes. Due to favorable equilibrium Fermi-level positions, the photoinduced electrons migrated to the rGO sheets, which then shuttled across the two-dimensional carbon network and were subsequently trapped by Pt active sites (path 2 in Fig. 7). The major reaction steps in the photocatalytic mechanism are summarized by Eqs. (2)–(8). The improved photoactivity on the Pt-GT could be attributed to the synergistic effect of Pt, rGO and TiO<sub>2</sub>, where rGO provided a large specific surface area and greatly increased the conductivity of electrons. In addition, GT served as a good support for achieving high dispersion of Pt, preventing them from serious aggregation and thus preserving their high catalytic performance. In comparison to Pt-TiO<sub>2</sub> binary nanocomposite, Pt-GT showed a marked enhancement in photoactivity, further justifying the significance of rGO as an effective catalyst mat for the Pt-TiO<sub>2</sub> photocatalyst (Fig. S10 in Supplementary Material).



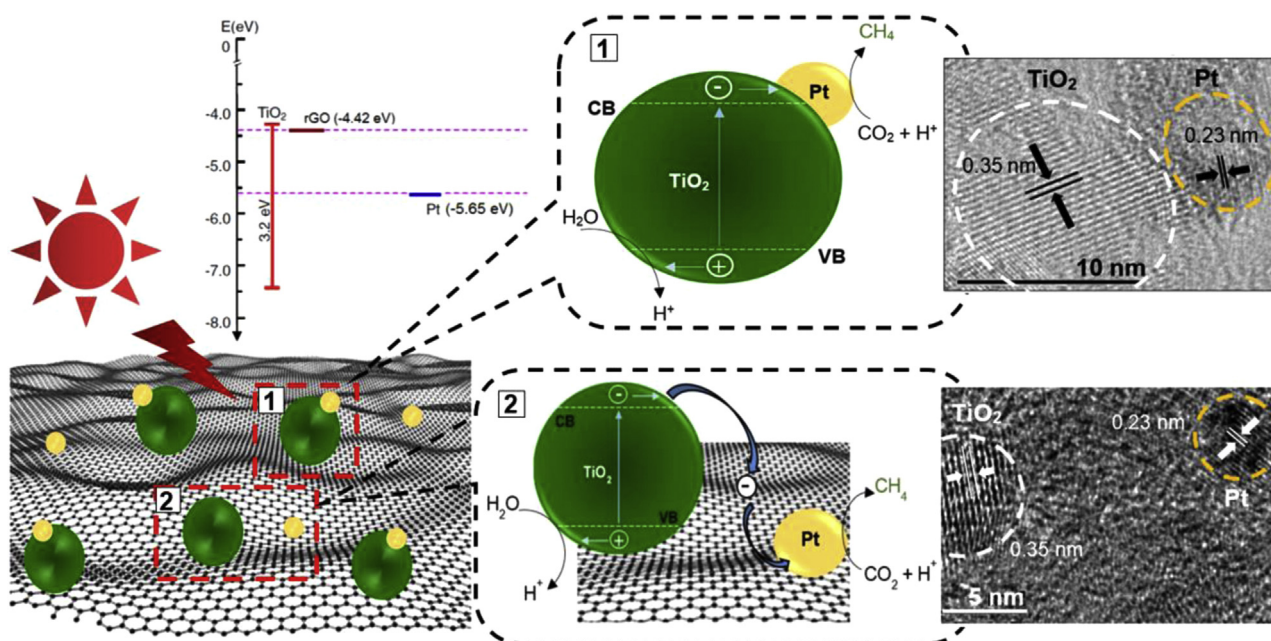
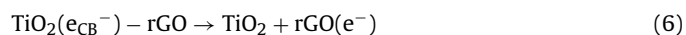


Fig. 7. Schematic illustrating the photoreduction of CO<sub>2</sub> to CH<sub>4</sub> over Pt-GT composite.



PL quenching effect is an efficient method to understand the emission mechanism and charge transfer within the material. The intensity of the PL spectrum is a direct measurement of the recombination rate of photogenerated electron–hole pairs, *i.e.* the faster the recombination occurs, the more intense the spectrum is. Alternatively, a lower intensity indicates that more photoinduced electrons are trapped and stably transferred through the interface. Therefore, the PL spectra of GT and NM-GT ternary nanocomposites can provide evidence to support the proposed photocatalytic mechanism and also elucidate the role of rGO and noble metal dopants in the TiO<sub>2</sub>-based composite systems. Fig. 8A demonstrates the representative PL spectra of pure anatase TiO<sub>2</sub>, GT and NM-GT ternary nanocomposites. The PL peak emission intensity was observed to follow the order: TiO<sub>2</sub> > GT > Au-GT > Ag-GT > Pd-GT > Pt-GT. After the formation of the binary composite of GT, the PL intensity of TiO<sub>2</sub> decreased markedly, highlighting the importance of rGO in lowering the recombination rate of electrons and holes. In the ternary nanocomposites, the PL intensity was found to have reduced further. As discussed earlier, this was attributed to the presence of Schottky barriers at the interface of each respective noble metal and the GT hybrid support, which served as an electron trap, thus hindering the recombination process. Notably, the Pt-GT composite showed the most significantly diminished PL intensity as compared to anatase TiO<sub>2</sub> and the other samples. This observation indicated the most efficient inhibition of charge carrier recombination in the Pt-GT sample. A comparative study of PL data and the photocatalytic experiments reveals that the obtained results are consistent with each other.

Similar to other types of dopants (*e.g.* non-metal, metal oxide, metal hydroxide *etc.*), there exists an optimum loading of noble metals to achieve most efficient photocatalytic performances. Therefore, the mass ratio of Pt to GT composites was varied from 0, 1, 2, 5 to 10 wt.% to determine the optimum loading for CO<sub>2</sub> reduction. The as-obtained samples were labeled as 0Pt-GT, 1Pt-GT, 2Pt-GT, 5Pt-GT and 10Pt-GT, respectively. As shown in Fig. 9,

the photocatalytic activity of CO<sub>2</sub> reduction was found to follow the order: 2Pt-GT > 1Pt-GT > 5Pt-GT > 10Pt-GT > GT. As discussed earlier, Pt doping exerts a variety of concentration-dependent effects on the surface of TiO<sub>2</sub>, where it not only extends the photoresponse of TiO<sub>2</sub> but also reduces charge recombination rate owing to its tendency to rapidly trap photogenerated electrons [68]. Among all the samples studied, 2Pt-GT exhibited the highest photocatalytic activity toward the reduction of CO<sub>2</sub>, where it achieved a total CH<sub>4</sub> yield of 1.70 μmol/g<sub>cat</sub> after 6 h of light irradiation. A decrease in

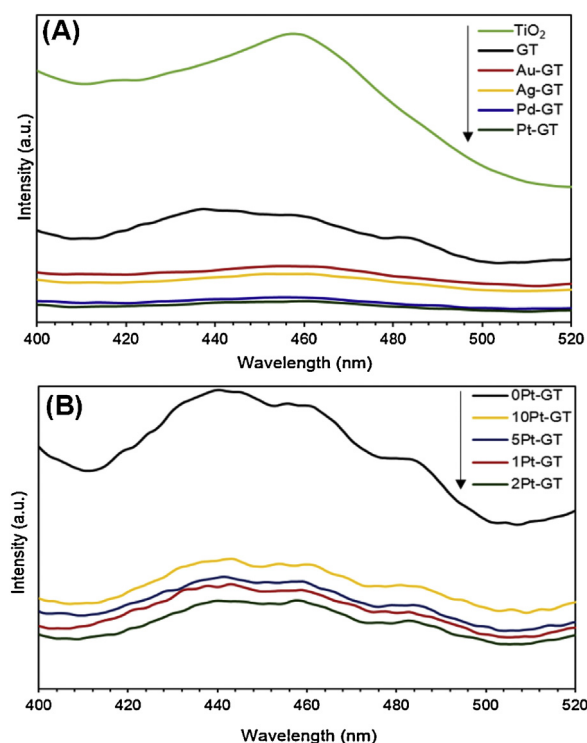


Fig. 8. PL spectra of (A) anatase TiO<sub>2</sub>, GT and NM (Pt, Pd, Ag, Au)-GT, (B) 0, 1, 2, 5, 10Pt-GT nanocomposites.

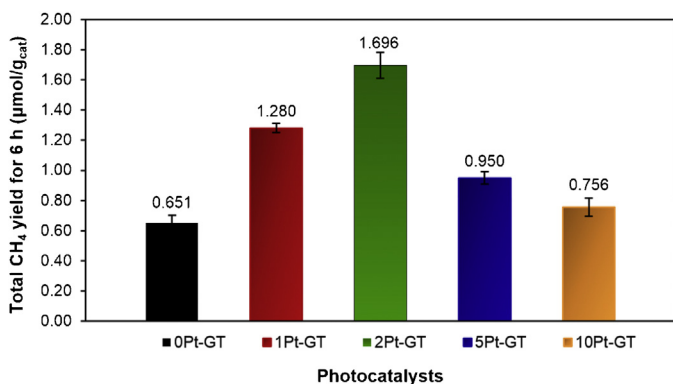


Fig. 9. Total yield of CH<sub>4</sub> over 0, 1, 2, 5 and 10Pt-GT attained after 6 h of reaction.

photocatalytic performance was observed for 1Pt-GT, where the total CH<sub>4</sub> yield was 1.28 μmol/g<sub>cat</sub>. It is suggested that the low content of Pt in the ternary composite did not contain sufficient electron trap sites to effectively hinder the recombination of electron-hole pairs, thus leading to its reduced photoactivity. Meanwhile, at higher loadings of Pt (5Pt-GT and 10Pt-GT), a decreasing trend in the photocatalytic performance was observed. Excess Pt doping has been reported to increase the negative charges on the surface of TiO<sub>2</sub> [62,69], which could promote the recombination of photogenerated holes, ultimately offsetting the charge separation effects of Pt. Furthermore, higher levels of Pt could have blocked the light absorption centers of TiO<sub>2</sub>, hence resulting in a decrease in photoactivity [36]. As shown in Fig. 8B, the highest PL quenching was observed for 2Pt-GT, which confirmed that there exists an optimum value for the amount of Pt to achieve the most efficient transportation of photoinduced electrons. The trend in the degree of PL quenching was well consistent with the photoactivity of 0, 1, 2, 5 and 10Pt-GT toward the photoreduction of CO<sub>2</sub> into CH<sub>4</sub>.

In the photocatalytic experiments, CH<sub>4</sub> was the only hydrocarbon product detected based on GC analysis. The distribution of products in the photoreduction of CO<sub>2</sub> is closely linked to the band structure of the photocatalyst and the redox potentials of the reduction-oxidation potentials of the products. The conduction band potential of TiO<sub>2</sub> has been reported to be −0.5 V [70], whereas the reduction potentials of the possible products are: CO<sub>2</sub>/CH<sub>4</sub>: −0.24 V [71,72]; CO<sub>2</sub>/CH<sub>3</sub>OH: −0.32 V [73]; CO<sub>2</sub>/COOH: −0.43 V [73]; CO<sub>2</sub>/CO: −0.52 V [74]. As the reduction potential for CH<sub>4</sub> production from CO<sub>2</sub> is lower than that needed for methanol, formic acid and carbon monoxide, CO<sub>2</sub> might have been preferably reduced to CH<sub>4</sub> over the NM-GT ternary composites. Meanwhile, molecular H<sub>2</sub> was also not detected by GC. It is likely that the photogenerated H• radicals and H<sub>2</sub> were rapidly consumed by CO<sub>2</sub> in the photoreduction process. Similar observations have also been reported by Li et al. [64] and in our previous communications [3,4,41,75].

#### 4. Conclusions

A series of ternary composites of noble metal (Pt, Pd, Ag, Au)-doped GT nanocomposites were successfully synthesized by a facile and environmentally benign polyol process while excluding the use of conventional harsh reducing agents. TEM observation revealed the uniformly distributed noble metals on the GT support. On the basis of diffuse reflectance spectra, the ternary composites were found to possess favorable optical properties for photocatalytic applications by enlarging the light absorption range. All noble metal-doped GT samples demonstrated an enhanced photocatalytic performance toward the reduction of CO<sub>2</sub> to CH<sub>4</sub> under visible light illumination. Among the noble metals studied, the

Pt-doped ternary composite (with 2.0 wt.% of Pt loading) demonstrated the best photoactivity, achieving a total CH<sub>4</sub> yield of 1.70 μmol/g<sub>cat</sub> after 6 h of light irradiation. The Pt nanoparticles played important roles in facilitating charge separation/transfer as well as expanding the absorption band further into the visible light region. This work opens up new possibilities in the development of new GT-based system photocatalysts with high performance in energy and environmental-related applications.

#### Acknowledgements

This work was funded by the Ministry of Education (MOE) Malaysia under the Fundamental Research Grant Scheme (Ref. no. FRGS/1/2013/TK05/MUSM/02/1) and Long-Term Research Grant Scheme (Acc. no. 2110226-113-00).

#### Appendix A. Supplementary data

Supplementary data associated with this article can be found, in the online version, at <http://dx.doi.org/10.1016/j.apcatb.2014.11.035>.

#### References

- [1] A. Yamasaki, J. Chem. Eng. Jpn. 36 (2003) 361–375.
- [2] S. Moret, P.J. Dyson, G. Laurenczy, Nat. Commun. 5 (2014) 4017.
- [3] L.-L. Tan, W.-J. Ong, S.-P. Chai, A.R. Mohamed, Chem. Commun. 50 (2014) 6923–6926.
- [4] W.-J. Ong, M.M. Gui, S.-P. Chai, A.R. Mohamed, RSC Adv. 3 (2013) 4505–4509.
- [5] J. Yu, Y. Wang, W. Xiao, J. Mater. Chem. A 1 (2013) 10727–10735.
- [6] C.Z. Wen, J.Z. Zhou, H.B. Jiang, Q.H. Hu, S.Z. Qiao, H.G. Yang, Chem. Commun. 47 (2011) 4400–4402.
- [7] W.-J. Ong, L.-L. Tan, S.-P. Chai, S.T. Yong, A.R. Mohamed, Nanoscale 6 (2014) 1946–2008.
- [8] W.-J. Ong, L.-L. Tan, S.-P. Chai, S.-T. Yong, A.R. Mohamed, ChemSusChem 7 (2014) 690–719.
- [9] J. Wang, P. Wang, Y. Cao, J. Chen, W. Li, Y. Shao, Y. Zheng, D. Li, Appl. Catal. B 136–137 (2013) 94–102.
- [10] M.S. Arif Sher Shah, K. Zhang, A.R. Park, K.S. Kim, N.-G. Park, J.H. Park, P.J. Yoo, Nanoscale 5 (2013) 5093–5101.
- [11] K. Woan, G. Pyrgiotakis, W. Sigmund, Adv. Mater. 21 (2009) 2233–2239.
- [12] C. Lee, X. Wei, J.W. Kysar, J. Hone, Science 321 (2008) 385–388.
- [13] L.-L. Tan, S.-P. Chai, A.R. Mohamed, ChemSusChem 5 (2012) 1868–1882.
- [14] A.A. Balandin, S. Ghosh, W. Bao, I. Calizo, D. Teweldebrhan, F. Miao, C.N. Lau, Nano Lett. 8 (2008) 902–907.
- [15] R.R. Nair, P. Blake, A.N. Grigorenko, K.S. Novoselov, T.J. Booth, T. Stauber, N.M.R. Peres, A.K. Geim, Science 320 (2008) 1308.
- [16] K.S. Novoselov, A.K. Geim, S.V. Morozov, D. Jiang, M.I. Katsnelson, I.V. Grigorieva, S.V. Dubonos, A.A. Firsov, Nature 438 (2005) 197–200.
- [17] C. Han, M.-Q. Yang, B. Weng, Y.-J. Xu, Phys. Chem. Chem. Phys. 16 (2014) 16891–16903.
- [18] X.-Y. Zhang, H.-P. Li, X.-L. Cui, Y. Lin, J. Mater. Chem. 20 (2010) 2801–2806.
- [19] N. Zhang, Y. Zhang, Y.-J. Xu, Nanoscale 4 (2012) 5792–5813.
- [20] M.-Q. Yang, N. Zhang, M. Pagliaro, Y.-J. Xu, Chem. Soc. Rev. (2014), <http://dx.doi.org/10.1039/c4cs00213j>.
- [21] M.-Q. Yang, Y.-J. Xu, Phys. Chem. Chem. Phys. 15 (2013) 19102–19118.
- [22] Y. Zhang, N. Zhang, Z.-R. Tang, Y.-J. Xu, ACS Nano 6 (2012) 9777–9789.
- [23] Q. Xiang, J. Yu, M. Jaroniec, Nanoscale 3 (2011) 3670–3678.
- [24] L.-L. Tan, W.-J. Ong, S.-P. Chai, A.R. Mohamed, Nanoscale Res. Lett. 8 (2013) 465–473.
- [25] H. Zhao, F. Su, X. Fan, H. Yu, D. Wu, X. Quan, Chin. J. Catal. 33 (2012) 777–782.
- [26] S.D. Perera, R.G. Mariano, K. Vu, N. Nour, O. Seitz, Y. Chabal, K.J. Balkus Jr., ACS Catal. 2 (2012) 949–956.
- [27] Y. Zhang, N. Zhang, Z.-R. Tang, Y.-J. Xu, Phys. Chem. Chem. Phys. 14 (2012) 9167–9175.
- [28] Y. Zhang, Z.-R. Tang, X. Fu, Y.-J. Xu, ACS Nano 5 (2011) 7426–7435.
- [29] Y. Zhang, Z.-R. Tang, X. Fu, Y.-J. Xu, ACS Nano 4 (2010) 7303–7314.
- [30] T.-D. Nguyen, C.-T. Dinh, T.-O. Do, Nanoscale 3 (2011) 1861–1873.
- [31] N. Zhang, M.-Q. Yang, Z.-R. Tang, Y.-J. Xu, ACS Nano 8 (2013) 623–633.
- [32] N. Zhang, Y. Zhang, X. Pan, M.-Q. Yang, Y.-J. Xu, J. Phys. Chem. C 116 (2012) 18023–18031.
- [33] W. Fan, Q. Zhang, Y. Wang, Phys. Chem. Chem. Phys. 15 (2013) 2632–2649.
- [34] Q. Zhai, S. Xie, W. Fan, Q. Zhang, Y. Wang, W. Deng, Y. Wang, Angew. Chem. 125 (2013) 5888–5891.
- [35] S. Xie, Y. Wang, Q. Zhang, W. Fan, W. Deng, Y. Wang, Chem. Commun. 49 (2013) 2451–2453.
- [36] B.K. Vijayan, N.M. Dimitrijevic, J. Wu, K.A. Gray, J. Phys. Chem. C 114 (2010) 21262–21269.



- [37] W. Zhao, C. Chen, X. Li, J. Zhao, H. Hidaka, N. Serpone, *J. Phys. Chem. B* 106 (2002) 5022–5028.
- [38] A.A. Ismail, D.W. Bahnemann, *Green Chem.* 13 (2011) 428–435.
- [39] Y.T. Liang, B.K. Vijayan, K.A. Gray, M.C. Hersam, *Nano Lett.* 11 (2011) 2865–2870.
- [40] A. Dhakshinamoorthy, S. Navalon, A. Corma, H. Garcia, *Energy Environ. Sci.* 5 (2012) 9217–9233.
- [41] W.-J. Ong, L.-L. Tan, S.-P. Chai, S.-T. Yong, A.R. Mohamed, *Nano Res.* 7 (2014) 1528–1547.
- [42] P. Wang, L. Han, C. Zhu, Y. Zhai, S. Dong, *Nano Res.* 4 (2011) 1153–1162.
- [43] B. Jiang, Y. Wang, J.-Q. Wang, C. Tian, W. Li, Q. Feng, Q. Pan, H. Fu, *ChemCatChem* 5 (2013) 1359–1367.
- [44] B. Liu, Y. Huang, Y. Wen, L. Du, W. Zeng, Y. Shi, F. Zhang, G. Zhu, X. Xu, Y. Wang, *J. Mater. Chem.* 22 (2012) 7484–7491.
- [45] A. Sánchez-Iglesias, E. Carbó-Argibay, A. Glaria, B. Rodríguez-González, J. Pérez-Juste, I. Pastoriza-Santos, L.M. Liz-Marzán, *Chem. Eur. J.* 16 (2010) 5558–5563.
- [46] Y. Lu, C. Shi, M.-J. Hu, Y.-J. Xu, L. Yu, L.-P. Wen, Y. Zhao, W.-P. Xu, S.-H. Yu, *Adv. Funct. Mater.* 20 (2010) 3701–3706.
- [47] Z.-C. Zhang, X. Zhang, Q.-Y. Yu, Z.-C. Liu, C.-M. Xu, J.-S. Gao, J. Zhuang, X. Wang, *Chem. Eur. J.* 18 (2012) 2639–2645.
- [48] Y. Wen, H. Ding, Y. Shan, *Nanoscale* 3 (2011) 4411–4417.
- [49] K. Ullah, L. Zhu, Z.-D. Meng, S. Ye, Q. Sun, W.-C. Oh, *Chem. Eng. J.* 231 (2013) 76–83.
- [50] P. Wang, Y. Ao, C. Wang, J. Hou, J. Qian, *J. Hazard. Mater.* 223–224 (2012) 79–83.
- [51] A.A. Ismail, R.A. Geioushy, H. Bouzid, S.A. Al-Sayari, A. Al-Hajry, D.W. Bahnemann, *Appl. Catal. B* 129 (2013) 62–70.
- [52] S.G. Leonardi, D. Aloisio, N. Donato, P.A. Russo, M.C. Ferro, N. Pinna, G. Neri, *ChemElectroChem* 1 (2014) 617–624.
- [53] G. Hu, F. Nitze, T. Sharifi, H.R. Barzegar, T. Wagberg, *J. Mater. Chem.* 22 (2012) 8541–8548.
- [54] Y. Chen, Y. Tang, S. Luo, C. Liu, Y. Li, *J. Alloys Compd.* 578 (2013) 242–248.
- [55] H. Gu, Y. Yang, J. Tian, G. Shi, *ACS Appl. Mater. Interfaces* 5 (2013) 6762–6768.
- [56] K.N. Kudin, B. Ozbaz, H.C. Schniepp, R.K. Prud'homme, I.A. Aksay, R. Car, *Nano Lett.* 8 (2007) 36–41.
- [57] Y. Wang, J. Yu, W. Xiao, Q. Li, *J. Mater. Chem. A* 2 (2014) 3847–3855.
- [58] A. Wood, M. Giersig, P. Mulvaney, *J. Phys. Chem. B* 105 (2001) 8810–8815.
- [59] K.T. Ranjit, T.K. Varadarajan, B. Viswanathan, *J. Photochem Photobiol. A* 96 (1996) 181–185.
- [60] G. Zhu, L. Pan, T. Xu, Q. Zhao, Z. Sun, *J. Alloys Compd.* 509 (2011) 7814–7818.
- [61] N. Yang, J. Zhai, D. Wang, Y. Chen, L. Jiang, *ACS Nano* 4 (2010) 887–894.
- [62] M.R. Hoffmann, S.T. Martin, W.Y. Choi, D.W. Bahnemann, *Chem. Rev.* 95 (1995) 69–96.
- [63] S. Ghasemi, A. Esfandiar, S. Rahman Setayesh, A. Habibi-Yangjeh, A. Irajizad, M.R. Gholami, *Appl. Catal. A* 462–463 (2013) 82–90.
- [64] X. Li, Z. Zhuang, W. Li, H. Pan, *Appl. Catal. A* 429–430 (2012) 31–38.
- [65] X. Zhang, Y.L. Chen, R.-S. Liu, D.P. Tsai, *Rep. Prog. Phys.* 76 (2013) 46401.
- [66] C. Clavero, *Nat. Photon.* 8 (2014) 95–103.
- [67] K. Mogyorósi, Á. Kmettykó, N. Czibrus, G. Veréb, P. Sipos, A. Dombi, *React. Kinet. Catal. Lett.* 98 (2009) 215–225.
- [68] W.N. Wang, W.J. An, B. Ramalingam, S. Mukherjee, D.M. Niedzwiedzki, S. Gangopadhyay, P. Biswas, *J. Am. Chem. Soc.* 134 (2012) 11276–11281.
- [69] H. Tahiri, Y.A. Ichou, J.-M. Herrmann, *J. Photochem Photobiol. A* 114 (1998) 219–226.
- [70] Y. Li, W.-N. Wang, Z. Zhan, M.-H. Woo, C.-Y. Wu, P. Biswas, *Appl. Catal. B* 100 (2010) 386–392.
- [71] W. Hou, S.B. Cronin, *Adv. Funct. Mater.* 23 (2013) 1612–1619.
- [72] N. Zhang, S. Ouyang, T. Kako, J. Ye, *Chem. Commun.* 48 (2012) 1269–1271.
- [73] C. Wang, R.L. Thompson, J. Baltrus, C. Matranga, *J. Phys. Chem. Lett.* 1 (2010) 48–53.
- [74] J. Yu, J. Jin, B. Cheng, M. Jaroniec, *J. Mater. Chem. A* 2 (2014) 3407–3416.
- [75] M.M. Gui, S.-P. Chai, B.-Q. Xu, A.R. Mohamed, *Sol. Energy Mater. Sol. Cells* 122 (2014) 183–189.